

An eclipsing M-dwarf close to the hydrogen burning limit from NGTS

Jack S. Acton¹,¹★ Michael R. Goad,¹ Sarah L. Casewell,¹ Jose I. Vines²,² Matthew R. Burleigh,¹ Philipp Eigmüller,³ Louise D. Nielsen⁴,⁴ Boris T. Gänsicke⁵,⁵ Daniel Bayliss⁵,⁵ François Bouchy,⁴ Edward M. Bryant,⁵ Samuel Gill,⁵ Edward Gillen^{6,7},^{6,7}† Maximilian N. Günther,⁸,⁸ James S. Jenkins⁹,⁹ James McCormac,⁵ Maximiliano Moyano,¹⁰ Liam R. Raynard¹,¹ Rosanna H. Tilbrook,¹ Stéphane Udry,⁴ Christopher A. Watson,¹¹ Richard G. West⁵ and Peter J. Wheatley⁵

¹*School of Physics and Astronomy, University of Leicester, University Road, Leicester LE1 7RH, UK*

²*Departamento de Astronomía, Universidad de Chile, Camino el Observatorio 1515, Las Condes, Casilla 36-D, 7591245, Santiago, Chile*

³*Institute of Planetary Research, German Aerospace Center, Rutherfordstrasse 2, D-12489 Berlin, Germany*

⁴*Geneva Observatory, University of Geneva, Chemin des Maillettes 51, CH-1290 Versoix, Switzerland*

⁵*Department of Physics, University of Warwick, Gibbet Hill Road, Coventry CV4 7AL, UK*

⁶*Astronomy Unit, Queen Mary University of London, Mile End Road, London E1 4NS, UK*

⁷*Astrophysics Group, Cavendish Laboratory, J.J. Thomson Avenue, Cambridge CB3 0HE, UK*

⁸*Department of Physics, and Kavli Institute for Astrophysics and Space Research, Massachusetts Institute of Technology, Cambridge, MA 02139, USA*

⁹*Centro de Astrofísica y Tecnologías Afines (CATA), Casilla 36-D, 7591245, Santiago, Chile*

¹⁰*Instituto de Astronomía, Universidad Católica del Norte, Angamos 0610, 1270709 Antofagasta, Chile*

¹¹*Astrophysics Research Centre, School of Mathematics and Physics, Queen's University Belfast, Belfast BT7 1NN, UK*

Accepted 2020 August 14. Received 2020 August 14; in original form 2020 June 23

ABSTRACT

We present the discovery of NGTS J0930–18, an extreme mass ratio eclipsing M-dwarf binary system with an early M-dwarf primary and a late M-dwarf secondary close to the hydrogen burning limit. Global modelling of photometry and radial velocities reveals that the secondary component (NGTS J0930–18 B) has a mass of $M_* = 0.0818^{+0.0040}_{-0.0015} M_\odot$ and radius of $R_* = 0.1059^{+0.0023}_{-0.0021} R_\odot$, making it one of the lowest mass stars with direct mass and radius measurements. With a mass ratio of $q = 0.1407^{+0.0065}_{-0.017}$, NGTS J0930–18 has the lowest mass ratio of any known eclipsing M-dwarf binary system, posing interesting questions for binary star formation and evolution models. The mass and radius of NGTS J0930–18 B is broadly consistent with stellar evolutionary models. NGTS J0930–18 B lies in the sparsely populated mass radius parameter space close to the substellar boundary. Precise measurements of masses and radii from single lined eclipsing binary systems of this type are vital for constraining the uncertainty in the mass–radius relationship – of importance due to the growing number of terrestrial planets being discovered around low-mass stars.

Key words: binaries: eclipsing – stars: low-mass.

1 INTRODUCTION

Eclipsing binary stars are of vital importance in the field of stellar structure. These are the only objects from which we are able to get accurate mass–radius measurements of stars to test against model predictions. This is particularly relevant for low-mass stars (known as M-dwarfs). Stars with masses below $0.25 M_\odot$ are the most common stellar objects (Henry et al. 2006) but despite this the physics governing them remains relatively poorly understood. In particular, the mass–radius relation for low-mass stars is poorly constrained when compared with theoretical models (Parsons et al. 2018).

Previous studies have shown that model predictions for masses and radii of M-dwarfs can differ from measured values by up to

10 percent (Feiden & Chaboyer 2012; Terrien et al. 2012). This discrepancy is most likely due to magnetic activity induced by interactions in short-period tidally locked binary systems (Ribas 2006; Chabrier, Gallardo & Baraffe 2007). However, this is not entirely clear due to the existence of longer period systems, which we would not expect to be tidally locked, that show the same over sizing as these short period systems (Doyle et al. 2011; Irwin et al. 2011), as well as short period systems that show good agreement with models (Blake et al. 2008). This is further complicated by the fact that it is expected that fully convective stars (those with masses $<0.35 M_\odot$) should show less inflation due to the nature of their atmospheres (Kraus et al. 2011).

It is then vital that we are able to further constrain models for low-mass stars by obtaining direct measurements of stellar masses and radii. This has motivated the search for examples of low-mass eclipsing binaries (also known as EBLMs) that have provided accurate mass and radius measurements for a large number of M-dwarf stars across a range of masses (e.g. Triaud et al. 2012; Gómez

* E-mail: ja466@le.ac.uk

† Winton Fellow.

‡ Juan Carlos Torres Fellow.

Table 1. Summary of observations.

Observation type	Telescope	Band	Cadence	Total integration time	Period	Notes
Photometry	NGTS	520–890 nm	13 s	156 nights	21/04/16–22/12/16	14 full eclipses
Photometry	SAAO	<i>I</i>	30 s	3 h	20/12/18	Single observation
Photometry	SAAO	<i>g'</i>	10 s	2.16 h	29/01/19	Single observation
Photometry	TESS	600–1000 nm	1800 s	28 d	02/02/19–27/02/19	10 eclipses in total
Spectroscopy	HARPS	378–691 nm	45 min	4.5 h	11/04/19–08/06/19	Six RV Points, EGGS mode

Maqueo Chew et al. 2014; Triaud et al. 2017; von Boetticher et al. 2017, 2019; Gill et al. 2019a). However, the lowest masses, between $0.1 M_{\odot}$ and hydrogen burning limit at $\sim 0.07 M_{\odot}$, remain relatively sparsely sampled.

When characterizing exoplanet systems, accurate knowledge of the host star’s parameters is crucial as these are used to determine the corresponding values for the planet. Uncertainties in the stellar values could lead to over or underestimation of discovered planetary masses and radii. This is of further importance as some of the most interesting planetary systems have been discovered around low-mass stars (e.g. Gillon et al. 2017; Günther et al. 2019; Kostov et al. 2019). The smaller radii of these stars mean that small planets produce transits of a much greater depth than the same planet occulting a larger star, making them much easier to detect in transit surveys. For this reason many modern transiting exoplanet surveys are designed to target such low-mass stars (e.g. TRAPPIST, Gillon et al. 2011; SPECULOOS, Delrez et al. 2018).

Additionally, observations of rare types of eclipsing binary systems can provide insights into star formation. For example, Wisniewski et al. (2012) proposed that there should be a lack of binaries with orbital periods less than 100 d with highly unequal mass components. There are examples of so-called extreme mass ratio binaries (EMRBs) comprising a large star (typically A or B spectral type) with an M-dwarf companion (e.g. Stevens et al. 2019), however, the vast majority of eclipsing M-dwarf binaries are systems of roughly equal mass (Delfosse et al. 2004). Laithwaite & Warren (2020) surveyed a large sample of late M-dwarf binaries and found that they are almost exclusively equal mass systems. This is possibly a formation effect. Bouchy et al. (2011) propose that stars with spectral types later than G have disc braking strong enough to cause low-mass short period companions to migrate inwards and become engulfed. Therefore, we would expect extreme mass ratio binaries of two low-mass stars to be rare.

In this paper, we present the discovery of NGTS J093016–185033.6 (hereafter NGTS J0930–18), a highly unequal mass ratio ($q = 0.14075$) eclipsing M-dwarf binary in which the secondary (NGTS J0930–18 B) is a very low mass star just above the classical hydrogen burning limit of $\sim 70 M_J$ (Dieterich et al. 2014). We make use of follow-up photometric and spectroscopic observations to determine accurate masses and radii for the star, which lies in a region of parameter space with few direct measurements. This discovery will aid in further constraining the lowest end of the stellar mass–radius relationship.

2 OBSERVATIONS

NGTS J0930–18 was initially discovered using photometry from NGTS (Wheatley et al. 2018). Follow-up observations were performed with the Sutherland High Speed Optical Cameras (SHOC; Coppejans et al. 2013) on the South African Astronomical Observatory (SAAO) 1-m telescope. This photometry was then used in conjunction with observations from the Transiting Exoplanet Survey

Satellite (TESS; Ricker et al. 2014). We obtained high-resolution spectra with HARPS (mounted on the ESO 3.6 m; Mayor et al. 2003) to determine the mass of the companion. These observations are detailed in Table 1 and described below.

2.1 NGTS

NGTS J0930–18 was initially identified in photometry from the Next Generation Transit survey (hereafter NGTS; Wheatley et al. 2018). NGTS is a wide-field photometric survey consisting of an array of 12 fully automated 20 cm telescopes operating at ESO’s Paranal observatory in Chile. The facility has been operational since early 2016, and is optimized for observations of K- and M-type stars, with sensitivity in the 520–890 nm wavelength range. NGTS has a wide field of view (instantaneously covering 96 deg^2) and delivers high-cadence (every $\sim 13 \text{ s}$) photometry with high precision (1 mmag per hour for an $I = 14 \text{ mag}$ star).

The optimization of NGTS for precise photometry of late spectral-type stars has allowed it to make several discoveries of interesting M-dwarf systems. These include the discovery of the most massive planet orbiting an M-dwarf (Bayliss et al. 2018) as well as the shortest period brown dwarf around a main-sequence star (in this case an early M-dwarf; Jackman et al. 2019). NGTS has also discovered M-dwarfs in double-lined eclipsing binaries (Casewell et al. 2018; Acton et al. 2020) and low-mass stars in long period orbits around stars of other spectral types (Gill et al. 2019b; Lendl et al. 2019). M-dwarf stars continue to be a key focus of the NGTS science program.

NGTS J0930–18 was observed during the 2016 NGTS observing season. The field containing the system was observed for 156 nights between 2016 October 17th and 2017 June 21st, and in total we obtained 185 227 10 s exposure science images. The magnitude of the system in various bandpasses, as well as positional information, is provided in Table 2. To allow for the detection of the system, the light curve was first cleaned using an implementation of the SysRem algorithm (Tamuz, Mazeh & Zucker 2005). Periodic signals that do not show a typical transit shape (such as those caused by stellar variability) were then automatically detected and removed. After cleaning the eclipses were detected using ORION (see Wheatley et al. 2018 for more information), an implementation of the BLS algorithm (Kovács, Zucker & Mazeh 2016).

ORION also calculated some initial parameters for the system, identifying a 2.3 per cent depth eclipse with a period of 1.33 d, which allowed the object to be identified as a candidate exoplanet. When phase-folded on the ORION identified period, we saw no evidence for a secondary eclipse at phase 0.5, implying that the companion must have a surface brightness that is significantly less than the primary star. Due to the lack of secondary eclipse and a transit depth that was consistent with a planetary companion, the object was followed-up photometrically and spectroscopically, where it was determined that the eclipsing object was in fact a low-mass stellar companion.

Four *Gaia* DR2 (*Gaia* Collaboration 2018) sources are present in the 15 arcsec radius photometric aperture used by the NGTS

Table 2. Stellar properties and colour magnitudes for NGTS J0930–18 obtained from *Gaia* DR2 (Gaia Collaboration 2018), NGTS (Wheatley et al. 2018), TIC v8 (Stassun et al. 2019), and 2MASS (Skrutskie et al. 2006).

Property	Value	Source
Gaia I.D.	DR2 5678383069566263552	<i>Gaia</i>
TIC I.D.	176772671	TIC v8
RA (J2000)	09:30:16.0	NGTS
Dec (J2000)	−18:50:33.62	NGTS
μ_α (mas yr ^{−1})	−30.528 ± 0.255	<i>Gaia</i>
μ_δ (mas yr ^{−1})	18.0662 ± 0.234	<i>Gaia</i>
Parallax (mas)	4.392 ± 0.140	<i>Gaia</i>
<i>G</i>	14.8357	<i>Gaia</i>
NGTS	13.98	NGTS
TESS	13.8995	2MASS
<i>V</i>	15.529	2MASS
<i>J</i>	12.701	2MASS
<i>H</i>	12.06	2MASS
<i>K_s</i>	11.869	2MASS

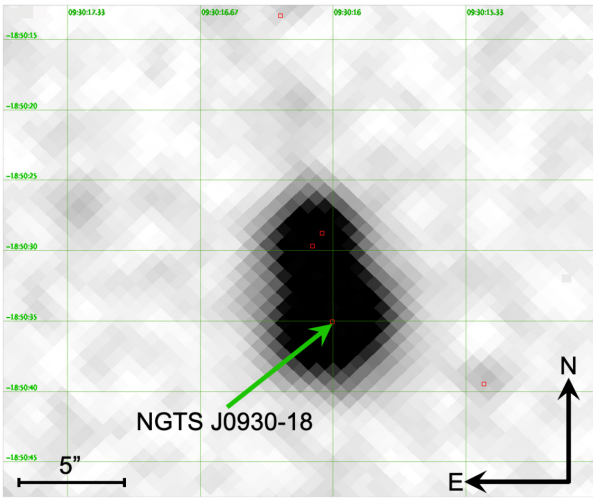


Figure 1. Digital Sky Survey (DSS) optical image of NGTS J0930–18. The red squares indicate the positions of identified *Gaia* DR2 sources. Four sources are present in the NGTS aperture which could contribute to the detection. NGTS J0930–18 is the larger southern star, which is physically associated with the smaller northern star.

pipeline, consequently we could not be certain which star was the source of the eclipses identified by ORION (see Fig. 1). Two of these stars are fainter than $G = 18$ (*Gaia* band), and therefore contribute negligible flux and cannot be the source of the signal seen in the NGTS data. The remaining two objects have the same parallax and proper motion, and therefore are a physically related pair, with the eclipse event occurring on one of these. To identify the source of the eclipse, we used the centroid vetting technique described in Günther et al. (2017) which allows the measurement of extremely small shifts in the flux centroid during eclipse. Using this technique, we identified a significant centroid shift indicating the southern star to be the eclipse source (*Gaia* ID – 5678383069566263552) – see Fig. 1.

NGTS observations captured 14 full eclipses of the system in total, as well as a large number of partial eclipses at the start or end of observing nights. The NGTS discovery light curve is shown in Fig. 2.

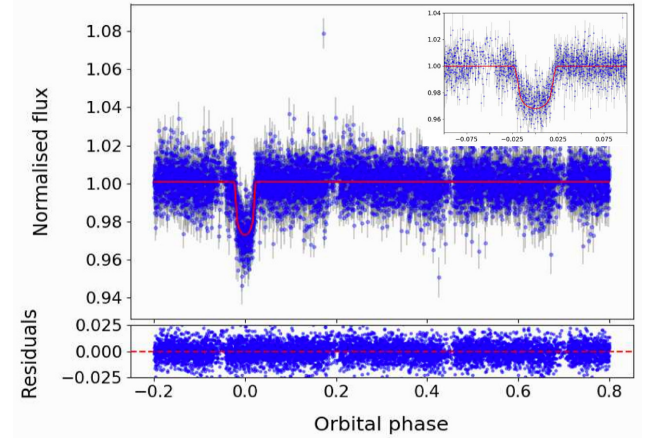


Figure 2. NGTS photometry of NGTS J0930–18 folded on a period of 1.33265 d and binned to 5 min. The red line shows the model fit obtained from joint modelling of photometric and spectroscopic data. Note that there is no obvious secondary eclipse at phase 0.5. Inset – zoomed-in plot of the primary eclipse of the system.

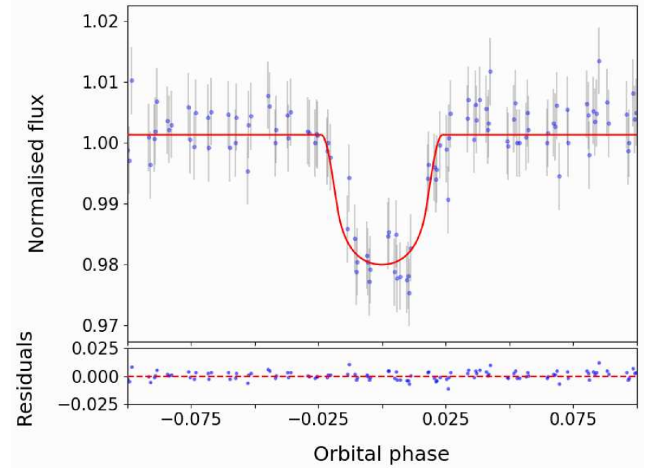


Figure 3. TESS 30-min cadence photometry of the eclipse of NGTS J0930–18 folded on the period of 1.33265 d. The red line shows the model fit obtained from joint modelling of photometric and spectroscopic data.

2.2 TESS

NGTS J0930–18 was observed in Sector 8 of the TESS mission (TIC-176772671, $T = 13.98$), which occurred between 2019 February 2nd and 2019 February 27th. These observations consist of standard full frame images taken with a cadence of 30 min. We extracted the photometry for NGTS J0930–18 from the full frame images of CCD 3 of camera 2. We used a custom aperture selected based on a flux threshold to minimize blending. However, due to the large TESS pixel size the blending is still greater than in the NGTS light curve. A floating median was applied to mask out systematic flux drops due to spacecraft effects. Further details of this method can be found in Gill et al. (2020).

The signal is clearly detected in the TESS data, with a total of seven eclipses captured by the TESS observations. A BLS search of the TESS data alone identifies a similar periodicity to the NGTS data, further validating this detection. The TESS light curve is shown in Fig. 3. As for the NGTS light curve, we see no evidence of a secondary eclipse, or significant out of transit variation in the light curve.

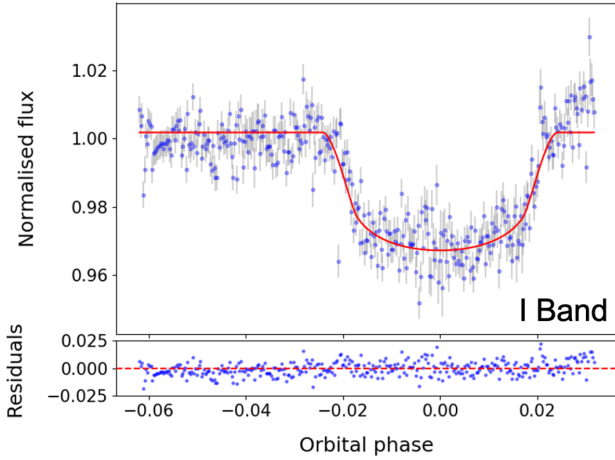


Figure 4. SAO 1 m/SHOC *I*-band photometry from the night 2018 December 20th showing a primary eclipse of NGTS J0930–18 plotted in phase. The red line shows the model fit obtained from joint modelling of photometric and spectroscopic data.

2.3 SAO photometry

We obtained photometry of NGTS J0930–18 using the SAO 1-m telescope equipped with the SHOC instrument (Copejans et al. 2013) on 2018 December 20th and 2019 January 29th in *I* and *g'* bands. The aim of the observation was to confirm transit depth and width and to refine the ephemeris for the system. Additionally, by obtaining multicolour photometry we can check for any wavelength dependent eclipse depth differences. The observations would also allow us to confirm which star is the source of the transit signal as they should be spatially resolved given the plate-scale of SHOC on the SAO 1-m telescope (0.167 arcsec per pixel, binned by a factor 4). The *I*-band observations consisted of $360 \text{ s} \times 30 \text{ s}$ exposures for a total observation time of 3 h. The *g'*-band observations were $770 \text{ s} \times 10 \text{ s}$ exposures for a total observing time of 7700 s ($\approx 2.13 \text{ h}$).

Standard bias and flat-fielding corrections were applied to the data using the local SAO SHOC pipeline, which is driven by PYTHON scripts running IRAF tasks (PYFITS and PYRAF). Aperture photometry was performed using the STARLINK package AUTOPHOTOM, which also measured and subtracted the sky background. The number of comparison stars and size of the aperture were chosen to minimize the rms scatter outside of the eclipse. For both sets of observations, we used a 4 pixel (2.67 arcsec) aperture with two stars used for comparison.

Both of these observations clearly detect the eclipse. The *I*-band observations detect a full eclipse of the system, whereas the *g'*-band observations capture the flux during eclipse as well as the egress. Additionally, the two brighter *Gaia* sources were able to be resolved. From this we were able to confirm that the eclipse occurred on the southern star, the brighter of the two possible eclipse sources, consistent with the result from centroid analysis. The light curves for each filter are shown in Figs 4 and 5. We note that there is not a significant difference in the eclipse depth between the two bands.

2.4 Radial velocity measurements

To determine the mass of the eclipsing object, NGTS J0930–18 was observed with the HARPS spectrograph on the ESO 3.6-m telescope (Mayor et al. 2003) under programme 0103.C-0719 (PI Bouchy). Due to the optical faintness of the object ($V = 15.30$), we used the

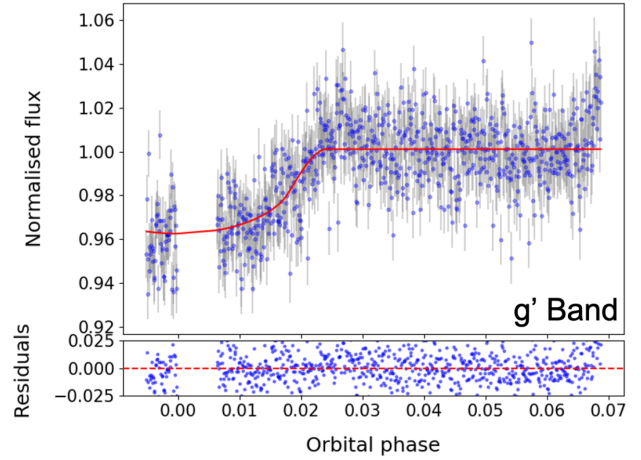


Figure 5. SAO 1 m/SHOC *g'*-filter photometry from the night 2019 January 29th of a primary eclipse of NGTS J0930–18 plotted in phase. The red line shows the model fit obtained from joint modelling of photometric and spectroscopic data. The data gap starting near phase 0.0 is due to passing clouds during the observations.

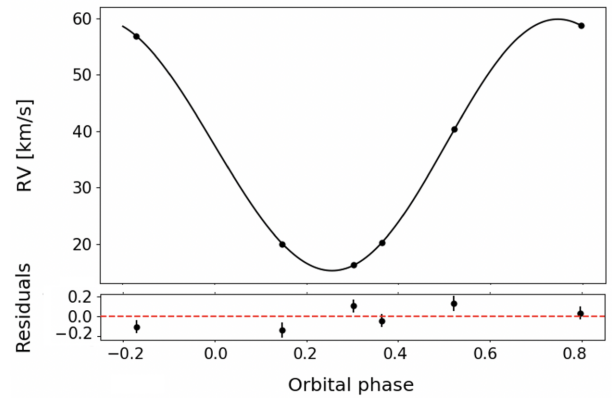


Figure 6. Phase-folded radial velocity curve for NGTS J0930–18 with black circles showing the six radial velocity measurements taken by HARPS between 2019 April 11th and 2019 June 8th. Radial velocities were phase folded on a period of 1.33265 d. The solid black line shows the model fit to the radial velocities obtained from global modelling of the system. Fit residuals (data model) are shown in the lower panel.

high efficiency (EGGS) mode, which uses a larger fibre in order to improve S/N at the expense of a modest reduction in spectral resolution. A total of six observations were taken between 2019 April 11th and 2019 June 8th, with all exposure times being 2700 s.

Observations were reduced using the standard HARPS data reduction pipeline. The spectra were cross-correlated with a template G2 stellar mask and the cross-correlation function (CCF) derived to determine the radial velocity of the star for each observation epoch. We used a G-type mask rather than an M-type as the star is rapidly rotating, and M-type masks struggle to deal with this. A single peak with large ($K \sim 22 \text{ km s}^{-1}$ scale) velocity shift was detected, consistent with a low-mass stellar companion. The radial velocities show a clear periodicity in phase with the period determined from photometric observations. The phase-folded radial velocity curve is shown in Fig. 6. We checked for correlation between bisector span and radial velocity and found no evidence for such correlation. The full radial velocity measurements are given in Table 3.

Table 3. Radial velocities for NGTS J0930–18.

BJD _{TDB} (–2450000)	RV (km s ^{–1})	RV error (km s ^{–1})	FWHM (km s ^{–1})	Contrast (per cent)
8584.6529	20.269	0.064	33.650	12.602
8585.6940	20.025	0.077	33.957	12.045
8586.6039	56.840	0.065	32.117	12.036
8638.5344	58.792	0.062	32.464	11.472
8640.5395	16.267	0.065	32.790	12.812
8643.4978	40.395	0.074	33.058	12.180

3 RESULTS

3.1 Primary star parameters

3.1.1 Spectral typing

In order to determine the spectral type of the primary star, NGTS J0930–18 A, we performed a template matching procedure. The HARPS spectra were wavelength shifted and then coadded to create a single higher signal-to-noise spectrum for analysis (SNR of 17). The spectral type was determined by comparing this spectrum with templates derived from Sloan Digital Sky Survey (SDSS) spectra covering a wide range of spectral types using the PYHAMMER code (Kesseli et al. 2017), a PYTHON implementation of the HAMMER spectral classification routine (Covey et al. 2007). PYHAMMER computes a chi-squared value that compares 34 spectral indices for each template, which are weighted relative to uncertainties in the individual observed spectra, to the corresponding values for the input spectrum. The spectral type that produces the minimum chi-squared value is taken as the assumed spectral type of the input star. The best matching template to our combined HARPS spectrum is that of an M0V star with [Fe/H] ~ 0 . We note, however, that the metallicity is not strongly constrained by these fits, with higher and lower metallicity templates also showing reasonable agreement with our spectrum.

3.1.2 Spectral analysis

An initial estimate of the stellar parameters for NGTS J0930–18 A was obtained using SPECMATCH-EMP (Yee, Petigura & von Braun 2017). These parameters would be used as priors when fitting the spectral energy distribution of the star to improve the quality of the result. SPECMATCH-EMP characterizes stars based on their optical spectra, making use of a substantial library of high-resolution ($R \sim 55\,000$), high S/N (> 100) spectra obtained using Keck/HIRES. These high-quality template spectra are used to classify an input spectrum (in this case the combined HARPS spectrum of NGTS J0930–18 A).

SPECMATCH-EMP effectively performs a two-step process. First, the input spectrum is shifted so that it is on the same wavelength scale as the library (template) spectra. This is achieved by performing a cross-correlation between the input spectrum and several reference spectra in turn for a predetermined wavelength region. The reference spectrum that gives the largest cross-correlation peak is then used to shift the entire spectrum.

Once the HARPS spectrum has been shifted to the appropriate wavelength range, the matching procedure is applied. The input spectrum is compared with every other star in the library (for a given wavelength range, e.g. Mg b triplet). $V \sin i$ is allowed to float, and a spline is fit to the continuum. The best matching stars to the input spectrum are identified using a chi-squared analysis. Linear combinations of the best matching spectra are then used to obtain an even better match than the individual best matching spectra alone. A

Table 4. NGTS J0930–18 A stellar parameters derived from SPECMATCH-EMP and ARIADNE. For the parameters derived by ARIADNE, the first error is the statistical error while the second is a systematic error calculated from the maximum difference between the average value and the values produced by the individual theoretical models.

Parameter	SPECMATCH-EMP	ARIADNE
T_{eff} (K)	4069 ± 70	$3982^{+15}_{-16} \pm 64$
$\text{Log } g$ (cm s ^{–2})	4.67 ± 0.12	$4.687^{+0.055}_{-0.055} \pm 0.045$
Radius (R_{\odot})	0.62 ± 0.10	$0.584^{+0.0094}_{-0.0103} \pm 0.020$
[Fe/H]	-0.01 ± 0.09	$-0.012^{+0.041}_{-0.046} \pm 0.085$
Mass (M_{\odot})	0.62 ± 0.08	$0.580^{+0.0092}_{-0.0063} \pm 0.017$
Age (Gyr)	9.89 ± 0.17	$9.20^{+2.20}_{-5.31} \pm 3.63$
Distance (pc)	—	$223.5^{+3.5}_{-3.0} \pm 4.5$

weighted average of the library parameters is then taken and used to determine the properties of the target star. For NGTS J0930–18 A these are given in Table 4.

Additionally, we measured the projected stellar rotation velocity ($v \sin(i)$) by fitting synthesized spectra using ISPEC (Blanco-Cuaresma et al. 2014). We fit only for $v \sin(i)$, fixing the other values to those obtained from SPECMATCH-EMP. This provides a value for the projected stellar rotation velocity of 30.17 km s^{-1} , showing that the star is rapidly rotating. Given the inclination determined in Section 3.2, this is consistent with the star being in a state of spin orbit synchronization.

3.1.3 SED fitting

We fit the spectral energy distribution (hereafter SED) of NGTS J0930–18 A using ARIADNE (Vines & Jenkins, in preparation). ARIADNE is a PYTHON tool that fits catalogue photometry to various atmospheric model grids. We fitted model grids from Phoenix v2 (Husser et al. 2013), BT-Settl, BT-Cond, BT-NextGen (Hauschildt, Allard & Baron 1999; Allard, Homeier & Freytag 2012), Castelli & Kurucz (2004), and Kurucz (1993). These were then convolved with various filter response functions.

Each model SED is created by interpolating the model grids in $T_{\text{eff}}\text{-log } g\text{-[Fe/H]}$ space. We also used distance, radius, and extinction in the *V* band as model parameters. Additionally, we include an excess noise term for each set of photometry to account for any underestimation of uncertainties. We applied priors for T_{eff} , $\text{log } g$, and [Fe/H] derived from the SPECMATCH analysis of the stacked HARPS spectrum (see Section 3.1.2). Priors for radius and distance were taken from *Gaia* DR2 and A_V was limited to the maximum line-of-sight value from the Schlegel, Finkbeiner & Davis (SFD) Galactic dust map (Schlegel, Finkbeiner & Davis 1998; Schlafly & Finkbeiner 2011). Excess noise parameters were normally distributed around zero with a variance equal to five times the size of the reported uncertainty.

Parameter estimation was performed using DYNESY's nested sampler for parameter estimation and calculating the Bayesian evidence for each model (Speagle 2020). ARIADNE then calculates the weighted average of each parameter using the relative probabilities of each of the fitted models. A mass estimate is then computed using MIST isochrones (Choi et al. 2016). A detailed explanation of ARIADNE is given in Vines & Jenkins (in preparation). The parameters for NGTS J0930–18 A derived by ARIADNE are given in Table 4 and a corner plot showing the posterior distribution of the key parameters is shown in Fig. 7.

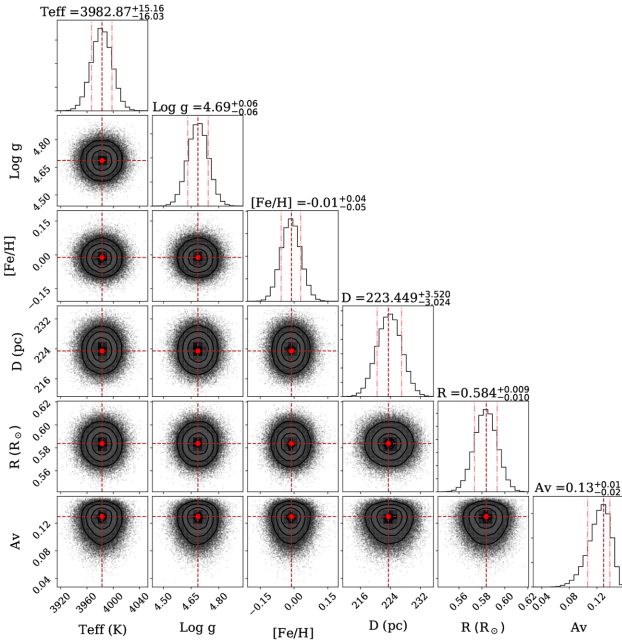


Figure 7. Cornerplot showing key primary star parameters derived using ARIADNE in Section 3.1.3.

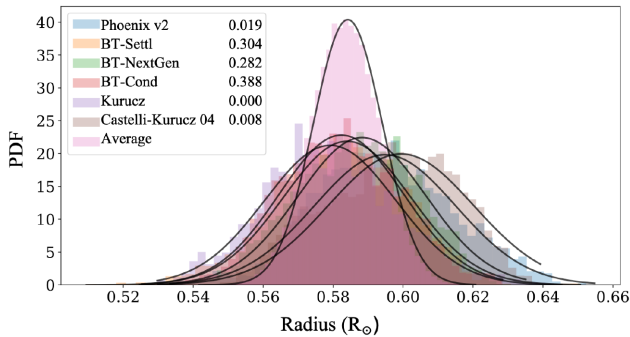


Figure 8. Histogram showing the probability distribution for the radius of NGTS J0930–18 A for each atmospheric model. The model probabilities are then used as weights to compute an overall average estimation, shown in pink, which has the best model value and uncertainty for the parameter.

We note that the method employed by ARIADNE leads to results with a remarkable degree of precision. This is a result of the mathematical treatment of the posterior parameter distribution. The distribution of each model is averaged, using the relative probabilities of each model as weights. This is determined using the following equation:

$$P(\theta_i) = \sum_{n=1}^N P(\theta | X, M_n) P(M_n | X), \quad (1)$$

where θ_i is the parameter to be averaged, $P(\theta|X, M_n)$ is the posterior distribution derived using Bayes theorem, and $P(M_n|X)$ is the Bayesian evidence of the individual model. This probability is used as a weight when averaging over the full set of models.

This results in higher precision than would be obtained by the use of any one model alone. The increased precision obtained by averaging over posterior distributions can be seen in Fig. 8, which shows the probability density function for the derived stellar radius. Preliminary testing has shown that ARIADNE obtains great accuracy

compared to radii derived by interferometry. This is particularly important due to the direct dependence of the mass and radius of the companion on that of the host.

To account for the effect of underestimating uncertainties when averaging over models, we also calculate a systematic error for the parameters derived by ARIADNE. As in Southworth et al. (2015), we determine this by fitting the SED with each model individually, and taking the largest difference between these individual values and the average value as the systematic error.

The values obtained with ARIADNE are more precise, but still consistent with those obtained by SPECMATCH-EMP. These parameters are roughly consistent with an early M-dwarf star of spectral type M0V, as determined in Section 3.1.1. We adopt the parameters derived by ARIADNE to derive the orbital solution as detailed in Section 3.2.

3.2 Global modelling

To determine the mass and radius of NGTS J0930–18 B, as well as other system parameters, we performed global fitting of both the photometric data (NGTS, TESS, and SAAO) and the HARPS radial velocities. This was performed using the eclipsing binary light-curve simulation code ELLC (Maxted 2016) in combination with the Markov chain Monte Carlo (MCMC) sampler EMCEE (Foreman-Mackey et al. 2013). Before performing this, we normalized the raw light curves by their median out of eclipse flux, and binned the NGTS data to 5 min to reduce computational time.

The walkers were initialized in a region of parameter space which provided a good initial fit. Each walker was then given a starting position selected from a normal distribution centred on these values. We used the values derived by ORION to obtain initial values for both the transit epoch and the orbital period. Initial values for the primary star radius, stellar radius ratio, impact parameter, light ratio, and radial velocity components were determined by first running the MCMC for a small number of steps to find values that gave a reasonable initial fit. We also incorporated a radial velocity jitter term added in quadrature in our modelling to account for stellar noise, as well as normalization scaling parameters and systematic errors for each of the four light curves. We additionally fit for a third light parameter to account for dilution in the NGTS and TESS light curves. We fixed this parameter to zero for the SAAO light curves due to the fact that the neighbouring star was not present in the aperture used for reduction.

Limb darkening parameters were obtained using the LDTK software (Parviainen & Aigrain 2015). A quadratic limb darkening law was used with stellar properties, e.g. T_{eff} and $\log g$ taken from the results given by ARIADNE. Limb darkening coefficients and uncertainties were calculated directly with LDTK, for each photometric filter used, and placed as priors for the fitting process.

An initial fit to the data resulted in an orbit with an eccentricity of $0.00592^{+0.0098}_{-0.0035}$. Lucy & Sweeney (1971) showed that many systems with low levels of eccentricity are actually circular orbits, where the addition of eccentricity has improved the fit due to the introduction of additional free parameters. Using the methods in Lucy & Sweeney (1971), we determine that there is an 83 percent probability that the measured eccentricity would be detected in a system with a true eccentricity of zero. Therefore, for the final system parameters we force a circular fit.

We used 200 walkers and 50 000 steps to model the light curve using the EMCEE sampler. Each walker used initial parameters that were randomized in a Gaussian ball around values previously determined to give a good initial fit. We note that alterations to our defined priors did not preclude the ability of the model to obtain

Table 5. Fitted and derived parameters for NGTS J0930–18. For parameters derived using values from ARIADNE, we also report a systematic uncertainty as described in Section 3.1.3.

Quantity	Description	Unit	Value	Error
Fitted parameters				
$\frac{R_{\text{pri}}}{a}$	Radius ratio of primary to semimajor axis	None	0.1243	+0.0023 –0.0016
k	Radius ratio of stars, $R_{\text{sec}}/R_{\text{pri}}$	None	0.1814	+0.0019 –0.0020
b	Impact parameter, $acos(i)/R_{\text{pri}}$	None	0.013	+0.095 –0.011
P	Orbital period	d	1.33264614	+0.00000126 –0.00000090
T_c	Epoch of primary eclipse centre	BJD	2457679.29957	+0.00053 –0.00057
σ_{NGTS}	Systematic error in NGTS light curve	Norm. flux	0.00593	+0.00010 –0.00012
σ_I	Systematic error in I light curve	Norm. flux	0.00454	+0.00027 –0.00040
$\sigma_{g'}$	Systematic error in g' light curve	Norm. flux	0.00838	+0.00062 –0.00063
σ_{TESS}	Systematic error in TESS light curve	Norm. flux	0.000045	+0.000330 –0.000051
β_{NGTS}	Normalized flux scale factor in NGTS data	None	1.000908	+0.000099 –0.000016
β_I	Normalized flux scale factor in I data	None	1.00086	+0.00036 –0.00044
$\beta_{g'}$	Normalized flux scale factor in g' data	None	1.00049	+0.00049 –0.00061
β_{TESS}	Normalized flux scale factor in TESS data	None	1.00155	+0.00030 –0.00019
u_{NGTS}	Linear LDC in NGTS band	None	0.499	+0.035 –0.026
u'_{NGTS}	Quadratic LDC in NGTS band	None	0.223	+0.039 –0.064
u_I	Linear LDC in I band	None	0.383	+0.038 –0.032
u'_I	Quadratic LDC in I band	None	0.434	+0.056 –0.071
$u_{g'}$	Linear LDC in g' band	None	0.500	+0.029 –0.036
$u'_{g'}$	Quadratic LDC in g' band	None	0.367	+0.066 –0.043
u_{TESS}	Linear LDC in TESS band	None	0.487	+0.030 –0.030
u'_{TESS}	Quadratic LDC in TESS band	None	0.175	+0.032 –0.025
K	Radial velocity semi-amplitude	km s ^{–1}	21.975	+0.404 –0.099
Γ_{pri}	Systemic velocity	km s ^{–1}	37.2464	+0.0070 –0.2443
σ_{RV}	Jitter in RV data	km s ^{–1}	0.287	+0.075 –0.260
Derived parameters				
R_{sec}	Radius of secondary	R_{\odot}	0.1059	+0.0023 –0.0021 (± 0.0040)
R_{sec}	Radius of secondary	R_J	1.052	+0.023 –0.021 (± 0.040)
m_{sec}	Mass of secondary	M_{\odot}	0.0818	+0.0040 –0.0015 (± 0.0052)
m_{sec}	Mass of secondary	M_J	85.7	+4.2 –1.5 (± 5.4)
q	Stellar mass ratio	None	0.1407	+0.0065 –0.0017 (± 0.0085)
a	Semimajor axis of system	au	0.02195	+0.00040 –0.00064 (± 0.00088)
i	Orbital inclination	deg	89.914	+0.085 –0.671
$T_{14\text{-pri}}$	Primary eclipse duration	h	1.510	+0.021 –0.026

a good fit. 10 000 steps were discarded as burn-in and not used when analysing the results of the modelling. The modal values of the posterior distributions were adopted as the most probable parameters, with the 68.3 per cent (1σ) highest probability density interval as the error estimates.

This global modelling resulted in mass and radius for NGTS J0930–18 B of $0.0818^{+0.0040}_{-0.0015} M_{\odot}$ ($85.7^{+4.2}_{-1.5} M_J$) and $0.1059^{+0.0023}_{-0.0021} R_{\odot}$ ($1.052^{+0.023}_{-0.021} R_J$). The binary has a notably low-mass ratio of just $0.1407^{+0.0065}_{-0.0017}$. The full list of best-fitting parameters derived from the posterior distributions are given in Table 5.

4 DISCUSSION

4.1 Unequal mass M-dwarf binaries

The results from SED fitting (Section 3.1.3) indicate that NGTS J0930–18 A has a mass of $0.5803^{+0.0092}_{-0.0063} M_{\odot}$ and a radius of

$0.584^{+0.0094}_{-0.010} R_{\odot}$ i.e. an early M-dwarf (Kaltenegger & Traub 2009). Thus, the system NGTS J0930–18 is an unequal mass eclipsing M-dwarf binary. This is an unusual configuration, as most known eclipsing M-dwarf systems (e.g. Parsons et al. 2018) are in near equal mass binaries. With a mass ratio of $0.1407^{+0.0065}_{-0.0017}$ NGTS J0930–18 is highly unusual. The mass ratio is more similar to the well-studied population of low-mass M-dwarfs in orbit around F-, G-, and K- stars (e.g. Triana et al. 2017) or transiting brown dwarf systems around early/mid M-dwarfs (e.g. Irwin et al. 2010; Johnson et al. 2011; Montet et al. 2015; Gillen et al. 2017; David et al. 2019).

It is expected that short-period M-dwarf systems with unequal mass components will be very rare. During formation, mass is preferentially accreted on to the lower mass component of the binary (Bate, Bonnell & Bromm 2002), which will over time drive the mass ratio towards unity and result in a system with roughly equal mass components. For short period, low-mass systems this effect is expected to be even greater due to dynamical effects. An early

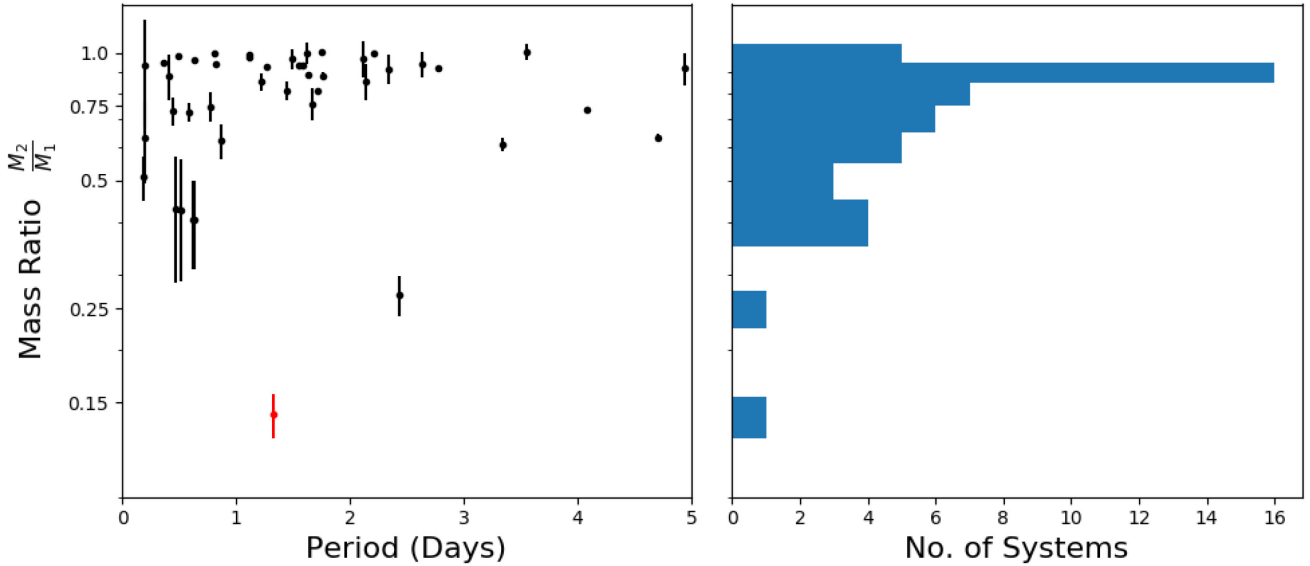


Figure 9. Left: Mass ratio as a function of period for M-dwarf binaries given by Parsons et al. (2018) and Nefs et al. (2013). NGTS J0930–18 is indicated in Red. Right: Histogram showing the distribution of M-dwarf binary mass ratios. NGTS J0930–18 is a clear outlier from the general population.

post-collapse star-forming cloud will fragment into a low number of multiple systems (Goodwin & Whitworth 2007). Dynamical decay and interactions within this collapsing cloud are biased against low-mass components, which are typically ejected on a short time-scale (Anosova 1986). In interactions with higher mass stars this means the low-mass star tends to be swapped with a higher mass replacement. Thus the mechanisms that produce short period binaries are biased to produce equal mass systems.

This theory is supported by observational evidence. Delfosse et al. (2004) surveyed a large number of M-dwarf binaries in the Solar neighbourhood. They found that for systems with a period less than 50 d, the distribution of the mass ratio peaked close to unity. The orbital period of NGTS J0930–18 is significantly shorter than this at 1.33265 d, meaning its formation and survival probes a sparse area of binary star parameter space. There are, however, examples of similar unequal mass binaries in the literature (e.g. Nefs et al. 2013).

In Fig. 9, we show the mass ratio as a function of period for short period (less than 5 d) systems with M-dwarf primaries taken from the samples in Parsons et al. (2018) and Nefs et al. (2013). From Fig. 9, it is clear that NGTS J0930–18 has the lowest mass ratio of any known M-dwarf binary system. This also demonstrates that the vast majority of short period systems of this type have a mass ratio close to 1, given the large cluster of systems in the top left of the plot. Such a short period system of two M-dwarfs with highly unequal masses is clearly unusual.

4.2 M-dwarf mass–radius relationship

The global modelling performed in Section 3.2 indicates NGTS J0930–18 B has a mass of $85.7^{+4.2}_{-1.5} M_J$. This places it just above the hydrogen burning mass limit of $\sim 70 M_J$ which separates brown dwarfs and low-mass stars (Baraffe et al. 1998). The mass and radius of the star are similar to that of TRAPPIST-1 (Gillon et al. 2017), demonstrating the importance of precise measurements in this parameter space to characterize current and future exoplanet discoveries.

In Fig. 10, we compare the mass and radius of NGTS J0930–18 B to a sample of low-mass stars as well as a model 10-Gyr stellar

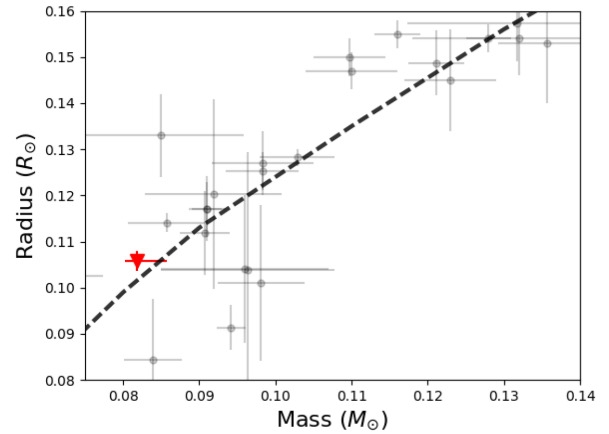


Figure 10. Comparison between NGTS J0930–18 B and a model stellar isochrone from Baraffe et al. (2015). The 10-Gyr isochrone is indicated by the black dashed line, and NGTS J0930–18 B by the red triangle. Similar M-dwarfs from Parsons et al. (2018), Triaud et al. (2020), and Mireles et al. (2020) are shown in black.

isochrone from Baraffe et al. (2015). Fig. 10 illustrates the low number of systems known in this parameter space. Most of the systems are from detections of low-mass secondary stars in eclipsing binaries with higher mass primaries, the same configuration as NGTS J0930–18. We also note the well-known scatter in the mass–radius relationship for low-mass stars is still present even at the lower end of the mass distribution.

This shows that the radius of NGTS J0930–18 B is very slightly inflated relative to models, but is still consistent to 1σ for its mass. Inflated radii of low-mass stars can often be associated with short orbital periods (Spada et al. 2013). This is due to the fact that at fast rotation speeds magnetic activity is enhanced that can affect convective processes, causing an inflation in stellar radius (Chabrier et al. 2007; López-Morales 2007). However, inflation of stellar radii has also been seen in longer period systems (e.g. Acton et al. 2020) indicating that this deviation is not consistent. Indeed, with a period

of just 1.33265 d we may have expected this object to show some level of inflation, which is not clearly seen. We note that the HARPS spectrum of the star shows clear H α emission, a strong indicator that the star is indeed magnetically active.

We note that direct detection of the secondary eclipse of this system to refine these parameters in the future will likely be difficult. The non-detection of a secondary eclipse in the NGTS data can be used to place an upper limit on the light ratio of the two stars. However, given the out of eclipse scatter a secondary eclipse would still not be detected even if NGTS J0930–18 B was more luminous than it actually is. For a 0.08 M_{\odot} dwarf with an age of 10 Gyr, Baraffe et al. (2015) give a temperature of 2345 K. From determining the surface brightness ratio for the system given the temperature of the primary determined in Section 3.1.3, we find the secondary eclipse depth to be around 0.25 percent, well within the scatter of both the TESS and NGTS light curves. An eclipse this shallow will be difficult to detect given the faintness of the system. Spectroscopic detection of a second set of lines associated with the secondary will also be difficult due to the rapid rotation of the star resulting in the blending of the spectral lines.

It is also important to note the precise mass and radius measurements obtained for NGTS J0930–18 B when compared with similar objects in Fig. 10. Owing to the high precision photometry and radial velocities used to characterize the system, we have derived the mass and radius of NGTS J0930–18 B to a precision of 5 per cent and 2 per cent, respectively. High precision measurements in this regime are vital for the empirical derivation of the mass–radius relationship stars at the lowest end of the mass–radius distribution.

5 CONCLUSIONS

We have discovered the M-dwarf eclipsing binary system NGTS J0930–18, with the secondary component, NGTS J0930–18 B, having a mass just above the hydrogen burning limit. We were able to determine a very precise mass and radius for NGTS J0930–18 B, and these parameters are of great scientific interest due to the prominence of very low mass stars in the search for temperate terrestrial exoplanets. Knowledge of the masses and radii of these stars are vital for characterization of future exoplanet discoveries, and these measurements can only be obtained precisely through the characterization of eclipsing binary stars similar to this system. NGTS J0930–18 B provides a valuable data point in a sparsely populated region of parameter space and will be of importance for future work in empirically deriving the mass–radius relationship for the lowest mass stars.

ACKNOWLEDGEMENTS

Based on data collected under the NGTS project at the ESO La Silla Paranal Observatory. The NGTS facility is operated by the consortium institutes with support from the UK Science and Technology Facilities Council (STFC) under projects ST/M001962/1 and ST/S002642/1.

This paper includes data collected by the TESS mission. Funding for the TESS mission is provided by the NASA Explorer Program.

This paper uses observations made at the South African Astronomical Observatory (SAAO). We thank Marissa Kotze (SAAO) for developing the SHOC camera data reduction pipeline.

This study is based on observations collected at the European Southern Observatory under ESO programme 0103.C-0719.

JA is supported by a Science and Technology Facilities Council (STFC) studentship. BTG, SG, and PJW acknowledge support

from STFC consolidated grants ST/L000733/1 and ST/P000495/1. MNG acknowledges support from MIT's Kavli Institute as a Juan Carlos Torres Fellow. JSJ acknowledges support by FONDECYT grant 1201371, and partial support from CONICYT project Basal AFB-170002. EG gratefully acknowledges support from the David and Claudia Harding Foundation in the form of a Winton Exoplanet Fellowship.

We thank the anonymous referee for their useful and constructive feedback to improve the paper.

DATA AVAILABILITY

The data underlying this article will be shared on reasonable request to the corresponding author.

REFERENCES

- Acton J. S. et al., 2020, *MNRAS*, 494, 3950
- Allard F., Homeier D., Freytag B., 2012, *Phil. Trans. R. Soc. A*, 370, 2765
- Anosova J. P., 1986, *Ap&SS*, 124, 217
- Baraffe I., Chabrier G., Allard F., Hauschildt P. H., 1998, *A&A*, 337, 403
- Baraffe I., Homeier D., Allard F., Chabrier G., 2015, *A&A*, 577, A42
- Bate M. R., Bonnell I. A., Bromm V., 2002, *MNRAS*, 332, L65
- Bayliss D. et al., 2018, *MNRAS*, 475, 4467
- Blake C. H., Torres G., Bloom J. S., Gaudi B. S., 2008, *ApJ*, 684, 635
- Blanco-Cuaresma S., Soubiran C., Heiter U., Jofré P., 2014, *A&A*, 569, A111
- Bouchy F. et al., 2011, *A&A*, 533, A83
- Casewell S. L. et al., 2018, *MNRAS*, 481, 1897
- Castelli F., Kurucz R. L., 2004, preprint ([arXiv:0405087](https://arxiv.org/abs/0405087))
- Chabrier G., Gallardo J., Baraffe I., 2007, *A&A*, 472, L17
- Choi J., Dotter A., Conroy C., Cantiello M., Paxton B., Johnson B. D., 2016, *ApJ*, 823, 102
- Coppejans R. et al., 2013, *PASP*, 125, 976
- Covey K. R. et al., 2007, *AJ*, 134, 2398
- David T. J., Hillenbrand L. A., Gillen E., Cody A. M., Howell S. B., Isaacson H. T., Livingston J. H., 2019, *ApJ*, 872, 161
- Delfosse X. et al., 2004, in Hilditch R. W., Hensberge H., Pavlovski K., eds, ASP Conf. Ser. Vol. 318, Spectroscopically and Spatially Resolving the Components of the Close Binary Stars. p. 166
- Delrez L. et al., 2018, in Marshall H. K., Spyromilio J., eds, Proc. SPIE Conf. Ser. Vol. 10700, Ground-Based and Airborne Telescopes VII. SPIE, Bellingham, p. 1070011
- Dieterich S. B., Henry T. J., Jao W.-C., Winters J. G., Hosey A. D., Riedel A. R., Subasavage J. P., 2014, *AJ*, 147, 94
- Doyle L. R. et al., 2011, *Science*, 333, 1602
- Feiden G. A., Chaboyer B., 2012, *ApJ*, 757, 42
- Foreman-Mackey D., Hogg D. W., Lang D., Goodman J., 2013, *PASP*, 125, 306
- Gaia Collaboration, 2018, *A&A*, 616, A1
- Gill S. et al., 2019a, *A&A*, 626, A119
- Gill S. et al., 2019b, *MNRAS*, 491, 1548
- Gill S. et al., 2020, *ApJ*, 898, L11
- Gillen E., Hillenbrand L. A., David T. J., Aigrain S., Rebull L., Stauffer J., Cody A. M., Queloz D., 2017, *ApJ*, 849, 11
- Gillon M., Jehin E., Magain P., Chantry V., Hutsemékers D., Manfroid J., Queloz D., Udry S., 2011, in EPJ Web Conf., 11, 06002
- Gillon M. et al., 2017, *Nature*, 542, 456
- Gómez Maqueo Chew Y. et al., 2014, *A&A*, 572, A50
- Goodwin S. P., Whitworth A., 2007, *A&A*, 466, 943
- Günther M. N. et al., 2017, *MNRAS*, 472, 295
- Günther M. N. et al., 2019, *Nature Astronomy*, 3, 1099
- Hauschildt P. H., Allard F., Baron E., 1999, *ApJ*, 512, 377
- Henry T. J., Jao W.-C., Subasavage J. P., Beaulieu T. D., Ianna P. A., Costa E., Méndez R. A., 2006, *AJ*, 132, 2360
- Husser T.-O., Wende-von Berg S., Dreizler S., Homeier D., Reiners A., Barman T., Hauschildt P. H., 2013, *A&A*, 553, A6

- Irwin J. et al., 2010, *ApJ*, 718, 1353
- Irwin J. M. et al., 2011, *ApJ*, 742, 123
- Jackman J. A. G. et al., 2019, *MNRAS*, 489, 5146
- Johnson J. A. et al., 2011, *ApJ*, 730, 79
- Kaltenegger L., Traub W. A., 2009, *ApJ*, 698, 519
- Kesseli A. Y., West A. A., Veyette M., Harrison B., Feldman D., Bochanski J. J., 2017, *ApJS*, 230, 16
- Kostov V. B. et al., 2019, *AJ*, 158, 32
- Kovács G., Zucker S., Mazeh T., 2016, Astrophysics Source Code Library, record ascl:1607.008
- Kraus A. L., Tucker R. A., Thompson M. I., Craine E. R., Hillenbrand L. A., 2011, *ApJ*, 728, 48
- Kurucz R. L., 1993, VizieR Online Data Catalog, 6039
- Laithwaite R. C., Warren S. J., 2020, preprint ([arXiv:2006.11092](https://arxiv.org/abs/2006.11092))
- Lendl M. et al., 2019, *MNRAS*, 492, 1761
- López-Morales M., 2007, *ApJ*, 660, 732
- Lucy L. B., Sweeney M. A., 1971, *AJ*, 76, 544
- Maxted P. F. L., 2016, *A&A*, 591, A111
- Mayor M. et al., 2003, *The Messenger*, 114, 20
- Mireles I. et al., 2020, *AJ*, 160, 133
- Montet B. T. et al., 2015, *ApJ*, 800, 134
- Nefs S. V. et al., 2013, *MNRAS*, 431, 3240
- Parsons S. G. et al., 2018, *MNRAS*, 481, 1083
- Parviainen H., Aigrain S., 2015, *MNRAS*, 453, 3821
- Ribas I., 2006, *Ap&SS*, 304, 89
- Ricker G. R. et al., 2014, in Oschmann Jr. J. M., Clampin M., Fazio G. G., MacEwen H. A., eds, *Proc. SPIE Conf. Ser. Vol. 9143, Space Telescopes and Instrumentation 2014: Optical, Infrared, and Millimeter Wave*. SPIE, Bellingham, p. 914320
- Schlaflly E. F., Finkbeiner D. P., 2011, *ApJ*, 737, 13
- Schlegel D. J., Finkbeiner D. P., Davis M., 1998, *ApJ*, 500, 525
- Skrutskie M. F. et al., 2006, *AJ*, 131, 1163
- Southworth J. et al., 2015, *MNRAS*, 454, 3094
- Spada F., Demarque P., Kim Y. C., Sills A., 2013, *ApJ*, 776, 87
- Speagle J. S., 2020, *MNRAS*, 493, 3132
- Stassun K. G. et al., 2019, *AJ*, 158, 138
- Stevens D. J. et al., 2019, preprint ([arXiv:1910.06212](https://arxiv.org/abs/1910.06212))
- Tamuz O., Mazeh T., Zucker S., 2005, *MNRAS*, 356, 1466
- Terrien R. C., Fleming S. W., Mahadevan S., Deshpande R., Feiden G. A., Bender C. F., Ramsey L. W., 2012, *ApJ*, 760, L9
- Triaud A. H. M. J. et al., 2012, *A&A*, 549, A18
- Triaud A. H. M. J. et al., 2017, *A&A*, 608, A129
- Triaud A. H. M. J. et al., 2020, *Nat. Astron.*, 4, 650
- von Boetticher A. et al., 2017, *A&A*, 604, L6
- von Boetticher A. et al., 2019, *A&A*, 625, A150
- Wheatley P. J. et al., 2018, *MNRAS*, 475, 4476
- Wisniewski J. P. et al., 2012, *AJ*, 143, 107
- Yee S. W., Petigura E. A., von Braun K., 2017, *ApJ*, 836, 77

This paper has been typeset from a $\mathrm{T}_{\mathrm{E}}\mathrm{X}/\mathrm{L}^{\mathrm{A}}\mathrm{T}_{\mathrm{E}}\mathrm{X}$ file prepared by the author.